# Effects of wind on the dynamics of the central jet during drop impact onto a deep-water surface

Xinan Liu,\* An Wang, and Shuang Wang<sup>†</sup>
Department of Mechanical Engineering, University of Maryland, College Park, Maryland 20742, USA

## Dejun Dai

First Institute of Oceanography, State Oceanic Administration, Qingdao, Shandong 266061, China



(Received 15 August 2017; published 14 May 2018)

The cavity and central jet generated by the impact of a single water drop on a deep-water surface in a wind field are experimentally studied. Different experiments are performed by varying the impacting drop diameter and wind speed. The contour profile histories of the cavity (also called crater) and central jet (also called stalk) are measured in detail with a backlit cinematic shadowgraph technique. The results show that shortly after the drop hits the water surface an asymmetrical cavity appears along the wind direction, with a train of capillary waves on the cavity wall. This is followed by the formation of an inclined central jet at the location of the drop impact. It is found that the wind has little effect on the penetration depth of the cavity at the early stage of the cavity expansion, but markedly changes the capillary waves during the retraction of the cavity. The capillary waves in turn shift the position of the central jet formation leeward. The dynamics of the central jet are dominated by two mechanisms: (i) the oblique drop impact produced by the wind and (ii) the wind drag force directly acting on the jet. The maximum height of the central jet, called the stalk height, is drastically affected by the wind, and the nondimensional stalk height H/D decreases with increasing  $\theta \operatorname{Re}^{-1}$ , where D is the drop diameter,  $\theta$  is the impingement angle of drop impact, and Re =  $\rho_a U_w D/\mu_a$  is the Reynolds number with air density  $\rho_a$ , wind speed  $U_w$ , and air viscosity  $\mu_a$ .

### DOI: 10.1103/PhysRevFluids.3.053602

# I. INTRODUCTION

The impact of water droplets on a deep-water surface in the presence of wind is a fundamental problem in nature. For instance, raindrops fall through a storm and impinge on the ocean and lake surface with oblique incidence angles from the vertical [1]. Large sea spray droplets produced from breaking waves in strong winds fall back to the ocean surface with various incidence angles to the wave surface [2,3]. However, little attention has been given due to numerous technical difficulties in the measurement and modeling of this complex phenomenon.

Normal drop impacts on a static liquid surface, herein corresponding to the case of no wind, have been extensively studied [4–17] and are usually classified into four regimes: floating, bouncing, coalescing, and splashing [18]. Different regimes may be determined by the relationship between the Weber number We =  $\rho U^2 D/\sigma$  and Froude number Fr =  $U^2/gD$ , where  $\rho$  is the drop density, U is the drop impact velocity, D is the drop diameter,  $\sigma$  is the surface tension, and g is the acceleration due to gravity. Generally speaking, at low Weber numbers, say, We < 10, the drops may float, bounce, or

<sup>\*</sup>xliu@umd.edu

<sup>†</sup>Present address: School of Artificial Intelligence, Xidian University, Xi'an, Shaanxi 710071, China.

coalesce, depending on the Froude numbers Fr. For a low Fr, the impacting drop floats on the target liquid surface before coalescing. As the Fr increases, the impacting drop bounces on the surface one or more times before coalescing. At even higher values of Fr, the impacting drops coalesce on impact with the target fluid.

When the We is greater than 10, the impacting drop coalesces with the formation of a crater, also called a cavity, below the water surface [9]. In this coalescence regime, a wave swell is raised around the site of the drop impact and spreads radially outward. At the same time, capillary waves that originate at the rim of the cavity propagate inward down the cavity wall and converge towards the center of the cavity. The transition between coalescence and splashing proceeds through a regime where bubble entrapment is coupled with a high-speed thin jet. While the bubble entrapment occurs because of the collapse of the wall in the cavity base [19], secondary droplets are generated from the tip of the thin jet. A vortex ring that propagates into the target liquid may also be observed. As the We increases, the capillary waves become steeper and the cavity forms a flat base before collapse. A thick jet appears after the collapse and later a large secondary droplet is ejected from the tip of the thick jet when the Fr number is high. Also, in the splashing regime, a thin liquid film, the so-called crown, is ejected upward at the periphery of the impinging site. The upper edge of the crown breaks up, ejecting small splash droplets due to various mechanisms of instability in terms of We and the Reynolds number  $Re = \rho U D/\mu$ , where  $\mu$  is the liquid viscosity [20].

The dynamics of the crater and central jet (also called a Rayleigh jet) generated by the normal impact of a drop onto a liquid surface has been studied by a number of researchers [21–24]. A theoretical model depicting the crater expansion has been developed in [21]. In the model, the flow around the crater is approximated by an irrotational velocity field past a moving and expanding sphere and the temporal evolution of the crater depth can be calculated by numerical solution of the governing equations of motion. A simpler model of the crater depth can also be found in [22]. As shown in the same articles, these models agree well with the experiments under certain drop impact conditions. The formation of the central jet by the collapse of a cavity has been experimentally investigated in [23]. Two regimes (singular jet and cavity jet) are identified with different generation mechanisms. In the singular jet regime, a fast thin jet is produced by the collapse of a singular capillary wave that sparks the whole jet dynamics. In the cavity jet regime with high Froude numbers, the jets created by the cavity retraction are fat and slow. In [24], it is shown that the breakup of central jets is controlled by the Weber number and a capillary time scale that depends on the Ohnesorge number Oh =  $\mu/\sqrt{\sigma\rho D}$ , the ratio of viscosity to surface tension force.

To some extent, drop impacts on the water surface in the presence of wind are analogous to oblique drop impacts [25–29]. In an experiment investigating oblique drop impact onto a deep-liquid pool, Ref. [30] identified three different impact regimes: smooth deposition onto the pool (coalescing), splashing in all directions, and splashing only in the direction of impact, based on the Weber number and drop impingement angle  $\theta$  (the angle between the velocity vector of the primary drop and the normal vector to the water surface). The coalescing of the oblique impact generated by a single drop on deep fluids has been experimentally studied in [31]. In this experiment, the impingement angle  $\theta$  ranges from 5.4° to 64.4° and the Weber number We ranges from 15 to 249. It is shown that the drop spreads on the target surface with no visible immersion of drop fluid into the target fluid for  $\theta < 23^{\circ}$  while a partial immersion of the drop fluid can be seen in the front part of the spreading drop or in the rear part of the impact crater for  $\theta > 23^{\circ}$ . Below a critical level of the Weber number We<sub>N</sub>, formed with the normal velocity component, capillary waves are produced on the drop and target surface in the early stage after impact. For  $We_N > 10$ , a lamella is ejected from the target surface. The formation of secondary droplets during oblique collision for  $7.2 \le We \le 818$  and  $11^{\circ} \le \theta \le 75^{\circ}$  has been experimentally investigated in [32]. It is found that when the impingement angle is less than 50°, the total mass of secondary droplets increases with increasing impingement angle. The increase in mass of the secondary droplets is likely due to the formation of a ship's prowlike asymmetric liquid sheet on the liquid surface after the collision. The prow tip is elongated to form a liquid column that breaks up and produces secondary droplets. However, no secondary droplet is observed when the angle exceeds 70°. Similar behaviors in more detail for each regime have been reported in the numerical simulations of oblique drop impacts on liquid films [33–36]. In addition, in a laboratory experiment investigating the bubble sound generated by single water drops striking the water surface with various oblique incidence angles, Ref. [37] demonstrated that the probability of a bubble formation is dramatically reduced as the angle of incidence becomes more oblique. The asymmetrical characteristics of the cavity created by the oblique drop impact have been discussed in [30]. It is shown that the cavity depth and its displacement with respect to the impact position primarily depend on the perpendicular and tangential Weber numbers, respectively. However, lacking in the literature is information regarding the central jet after the oblique impact of a drop onto a liquid surface.

Recently, there have been several publications studying normal drop impact on moving liquid films [36,38–42]. The experiment of a single drop impacting on a flowing liquid thin film given in [38] shows that a liquid sheet forms where the drop spreading direction is opposite to the film flow. Small droplets are generated from the top rim of the liquid sheet. The experimental results given in [39] showed that the outcomes of normal droplet impact on moving films exhibit nearly the same regimes for the impact on stationary liquids but with different transition boundaries. The flow patterns of a normal drop impact on a moving wet wall are compared with that of an oblique drop impact on a stationary wet wall in [36] by means of numerical simulation.

The main objective of the present study is to understand better the physics of the impact of single water drops on a planar water surface in the presence of wind. This paper focuses on the effects of wind on the dynamics of the cavity (crater) and central jet (stalk) generated by the drop impact, while the crown and secondary droplets generated from the crown rim were reported in [43]. These parameters are important to the measurement of radar backscattering from a water surface in rain fields [44,45]. It should be mentioned that the dynamics of a drop impact onto deep water in the presence of wind are much more complicated than that of an oblique drop impact onto a static liquid pool and a normal drop impact on a moving liquid surface. First, as the drop falls in the wind field, the wind adds a horizontal component to the impact velocity, resulting in an oblique drop impact. This oblique impact in turn affects the dynamics of the cavity and central jet. Second, the wind exerts a drag force on the splashing outcomes that appear above the water surface. Third, the wind generates surface waves and surface wind drift. The surface waves alter the impingement angle to the local water surface, while the surface wind drift modifies the underneath flow field of the drop impact. In the present experiments, an effort to minimize the influences of surface waves and surface wind drift is given by positioning the drop impacts at a very short wind fetch varying approximately from 15 to 25 cm. Still, other effects that occur concurrently have to be considered in exploring the physics of the drop impact in the presence of wind. This work can be applied to the field of the impact of drops on deep-liquid surfaces.

The remainder of this paper is organized as follows. Section II describes the experimental setup. The results and discussion are presented in Sec. III. A summary and prospects for future work are given in Sec. IV.

### II. EXPERIMENTAL SETUP

The experiment was carried out in a wind tunnel with a test section that is 0.61 m in length and  $0.31 \times 0.31 \,\mathrm{m}^2$  in cross section see [Fig. 1(a)]. The test section is made of a clear plexiglass acrylic sheet for imaging purposes. The floor of the test section sinks by 15.3 cm below the bottom of the entrance of the wind tunnel and the indentation is filled with distilled water to create a deep-water pool. The air flow in the tunnel is driven by a variable-speed fan and conditioned by a honeycomb and two screens that are placed inside the settling chamber at the entrance of the wind tunnel. The wind velocity profile in the wind tunnel  $[U_{\mathrm{wind}}(z)]$ , where z is the vertical distance from the surface of the water pool] is measured with a Pitot tube as baseline data. The Pitot tube is mounted on a vertical traverser and positioned in the vertical center plane of the test section at the location of drop impacts. A differential capacitance manometer (Type 120 made by MKS, Inc.) is connected to the Pitot tube to display the difference between the static and stagnation pressures and Bernoulli's

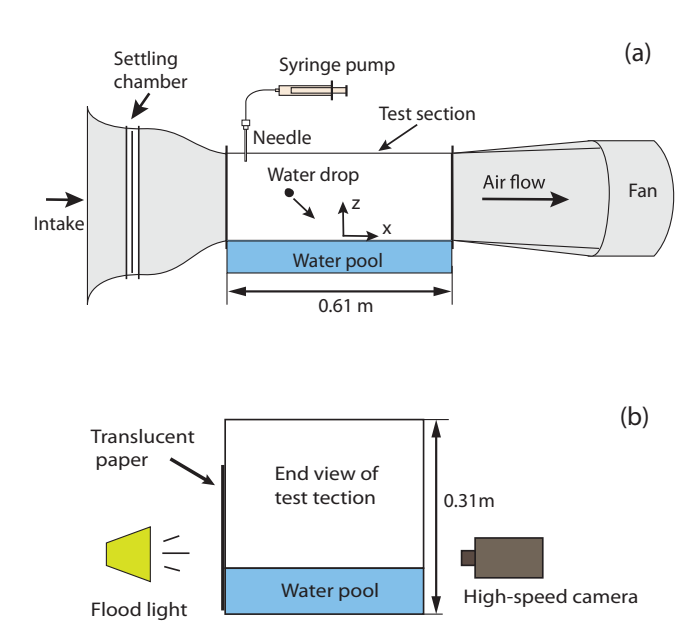


FIG. 1. Schematic showing (a) the facility for single-drop impact experiments and (b) the setup of the high-speed camera and light in the lateral perspective (end view).

equation is used to calculate the wind velocity at each height. Figure 2 shows plots of  $U_{\rm wind}$  versus z for four wind conditions used in the present study. As can be seen from the figure, near the water surface, a thin boundary layer forms for each wind condition and the thickness of this boundary layer ranges from 10 mm for the lowest wind speed to 20 mm for the highest wind speed and increases as the wind velocity increases. Above this boundary layer, a uniform wind with velocity ranging from

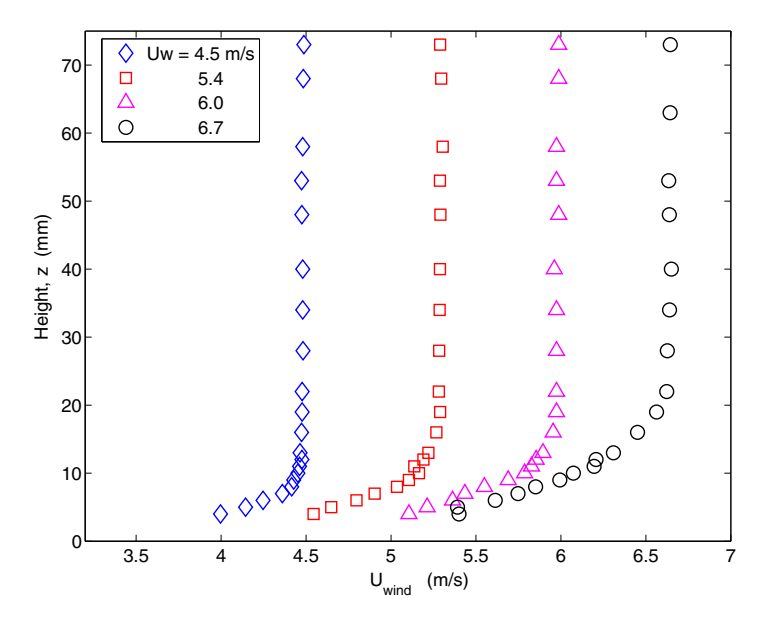


FIG. 2. Wind velocities versus the height above the water surface (z = 0) at the locations of drop impacts in the test section of the wind tunnel.

4.5 to 6.7 m/s is formed in the wind tunnel. In the remainder of this paper, each wind condition is represented by this uniform wind speed, denoted by  $U_w$ . The weak water flow field induced by wind in the pool is measured by a particle image velocimetry system. The horizontal velocities near the water surface are less than 1 cm/s and have little variations from one wind speed to another. Further details about the wind tunnel and test section can be found in [43].

A vertically oriented hypodermic needle with the tip ground flat and polished is used to generate impacting water drops, also defined as primary drops. The hypodermic needle pierces the top of the test section and is connected to a programmable syringe pump which is filled with distilled water. A very slow pumping rate is used so that water drops are steadily created at the tip of the hypodermic needle, primarily due to the effects of gravity and surface tension. After leaving the needle, the drops fall with no initial velocity and are convected by the wind before hitting the water surface of the pool. The release height of the needle tip above the water surface is 0.254 m.

The primary water drops in the air, and cavities and stalks (central jets) generated at the air-water interface during the drop impact are visualized with a backlit cinematic shadowgraph technique that uses a high-speed camera (Phantom V640, Vision Research Inc). The camera observes in the lateral perspective [see Fig. 1(b)] and the objective of the camera has a focal length of 200 mm. Illumination for imaging is provided by a 500-W halogen lamp at the opposite side of the test section. A piece of translucent paper is attached to the wall of the test section near the light source for a uniform background intensity. The camera records the events in high-speed movies with a frame rate of 1000 images per second. The contour profiles of the primary water drops in the air and the surface contours of craters below the water surface and stalks above the water surface are extracted from each image in these high-speed movies with gradient-based edge detection methods as described in [46]. It should be mentioned that the focal depth of the low part of the image below the free water surface is slightly different from that above the free surface because of the refraction index of water. The pixel resolutions of the image for the portion below and above the free water surface are 45 and 42.2 pixels/mm, respectively.

The primary drop diameter D is calculated using the projected drop area A and circumference P, with D = 4A/P, from the images extracted from high-speed movies. Note that drops produced from a needle and traveling in the wind field are found to be variable in size and asymmetrical and skewed in certain directions prior to the moment of impact. To eliminate the effect of these uncertainties on the results presented below, the initial condition of each primary drop is set at the moment of its impact instead of leaving the tip of the needle. The size and shape of the primary drop are measured from the image one frame prior to the impact in each experimental run and these measurements are used in calculating all dimensionless parameters, including We, Fr, Re, and Oh. As for the primary water drops with diameter in the range from 2.50 to 4.11 mm, the uncertainties of their diameters in the wind field and in the air (no wind) are  $\pm 0.04$  and  $\pm 0.03$  mm (the measurement errors are about 1.6% and 1.2%), respectively. The projection of the impacting drop is fitted with an ellipse formula and the minor to major axis ratio ranges from 0.86 to 0.99, with an average of 0.93 and a standard deviation of 0.045. It is known that the geometry of the cavity for a normal impact can be affected by the prolate form of the impacting drop with a large major-to-minor axis ratio [47,48]. In the current experiments, the angles between the major axis of the impacting drop and the free water surface in the wind field are mainly less than 45°, indicating that the primary drop at the moment of the impact may be considered as the oblate form. Also, only slight variations on the ratio of the maximum depth and diameter of the cavity from run to run are observed in the wind field and the variations do not affect the conclusions drawn in the latter part of the present paper.

The impact velocity of the primary drop is calculated from the drop positions recorded in the two consecutive images prior to the impact. Figure 3 shows the horizontal and vertical impact velocities of primary water drops versus the drop diameter under various wind conditions. In the figure, each data point represents one experimental run. Three or four repeated runs are taken for each experimental condition. The three lines in Fig. 3(a) correspond to three different needle sizes with gauge 15, 18, and 21 (corresponding to external diameters of 1.83, 1.27, and 0.81 mm), respectively. As can be seen from Fig. 3(a), for each needle, the horizontal impact velocity u increases with increasing wind

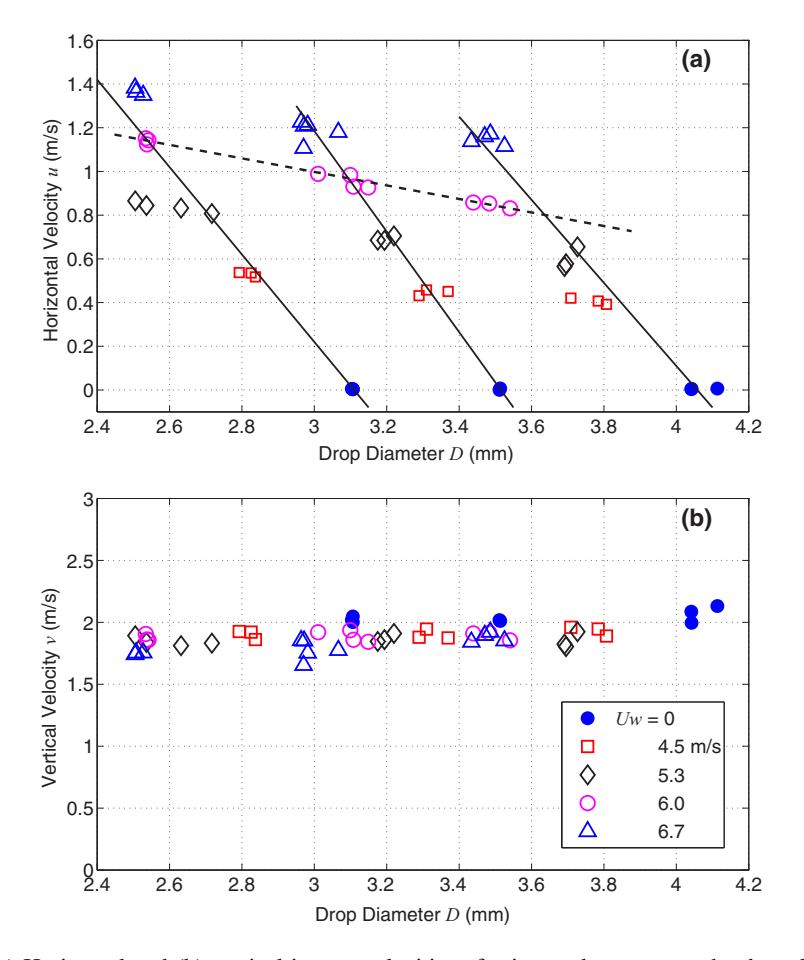


FIG. 3. (a) Horizontal and (b) vertical impact velocities of primary drops versus the drop diameter with various wind speeds. The three solid lines in (a) correspond to three different size needles, while the dashed line refers to  $U_w = 6.0 \text{ m/s}$ .

speed. Since the tip of the needle is in the wind field, the diameter of the primary drop decreases as the wind speed increases and a wider range of primary drop diameters is obtained. However, the dependence of drop diameter on wind speed is not considered in the present study. For a given wind speed, the horizontal impact velocity of the drop decreases as the drop diameter increases (denoted by the dashed line) under the effect of the drag force of the wind [see Eq. (A2)]. Figure 3(b) shows that the vertical impact velocities v of droplets are nearly the same (about 2.0 m/s) because the same release height (h = 0.254 m) is used for all experimental conditions. This v value is lower than that computed with  $\sqrt{2gh} = 2.23$  m/s from conversion of potential energy into kinetic energy due to the vertical air-drag force acting on the drop, as in Eq. (A3). The slight increase of v with increasing drop diameter shown in Fig. 3(b) is consistent with Eq. (A3), which demonstrates the influence of drop diameter on the vertical acceleration of the primary drop (see the Appendix).

#### III. RESULTS AND DISCUSSION

As baseline data, Fig. 4 shows eight images obtained from a high-speed movie of the impact of a drop with a diameter of D = 3.5 mm without wind. These images were recorded in the lateral perspective and demonstrate the sequence of events commonly taking place during the normal impact

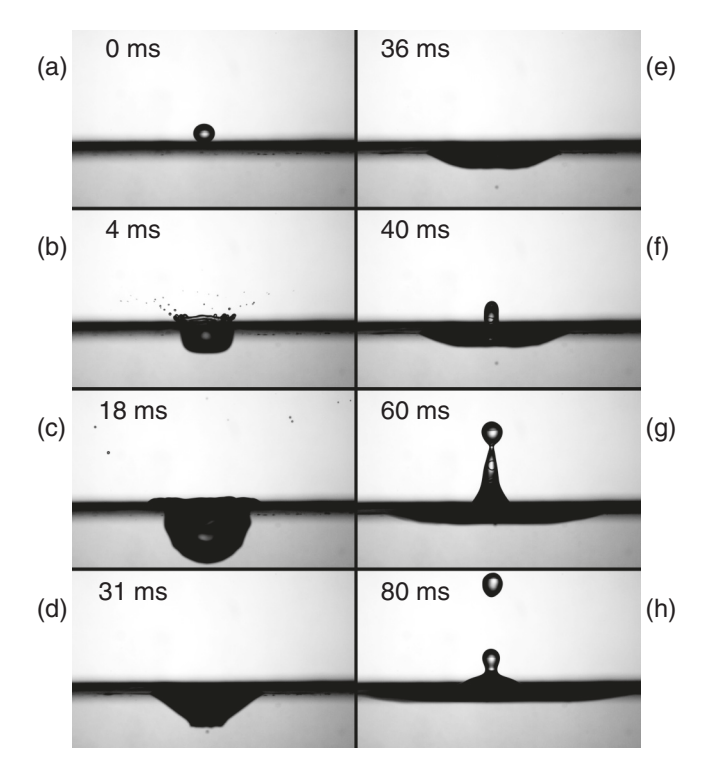


FIG. 4. Images from a high-speed movie of the normal impact of a single drop on the deep-water surface in the lateral perspective. Each image shows a  $48.2 \times 30.1 \text{ mm}^2$  section. The diameter of the primary drop D=3.5 mm, the impact velocity U=2.0 m/s, We = 192, and Fr = 117. (a) The drop is about to collide with the water surface (t=0 ms); (b) a crown forms above the water surface while a cavity with a flat base appears underneath the water surface in a short time (t=4 ms) after the drop impact and secondary droplets are generated from the crown top; (c) the cavity expands outward and downward to a maximum depth (t=18 ms); (d) the crater retreats upward and forms a cone shape with a bubble generation underneath the bottom of the crater (t=31 ms); (e) the crater vanishes (t=36 ms); (f) a stalk (central jet) forms at the center of the impact site (t=40 ms); (g) the stalk rises to its maximum height with a droplet forming on the tip (t=60 ms); and (h) a large secondary droplet is ejected from the tip of the stalk and moves upward until the maximum height (t=80 ms).

of a single drop on a quiescent water surface. As can be seen from Fig. 4, a crown forms in a short time (t = 4 ms) after a flared film of liquid is thrown upward and outward from the periphery of the colliding region. Secondary droplets are generated from the tips of fingers that shoot out from the upper part of the film. While the crown forms above the water surface, a crater (also called cavity) with a flat bottom appears below the level of the original free water surface. The cavity continues to enlarge downward and soon takes the shape of a hemisphere as it reaches its maximum depth [Fig. 4(c), t = 18 ms]. The cavity then stops growing downward and starts to retreat. At this moment, capillary waves that are generated from the rim of the impact cavity start to spread downward along the cavity wall and thus distort the shape of the cavity into that of a flat-bottomed cone. A small bubble forms at the bottom of the crater [Fig. 4(d), t = 31 ms]. At t = 36 ms [Fig. 4(e)], the crater disappears and later, a central jet, the so-called stalk, starts to form at the center of the impact location [Fig. 4(f), t = 40 ms]. This stalk moves upward until its highest point [t = 60 ms in Fig. 4(e)]. At this moment, a water droplet that is much larger than those secondary droplets mentioned above is ejected from the tip of the stalk. The water droplet continues to move upward until its highest point [t = 80 ms in Fig. 4(f)] and the remaining part of the stalk falls back to the water surface.

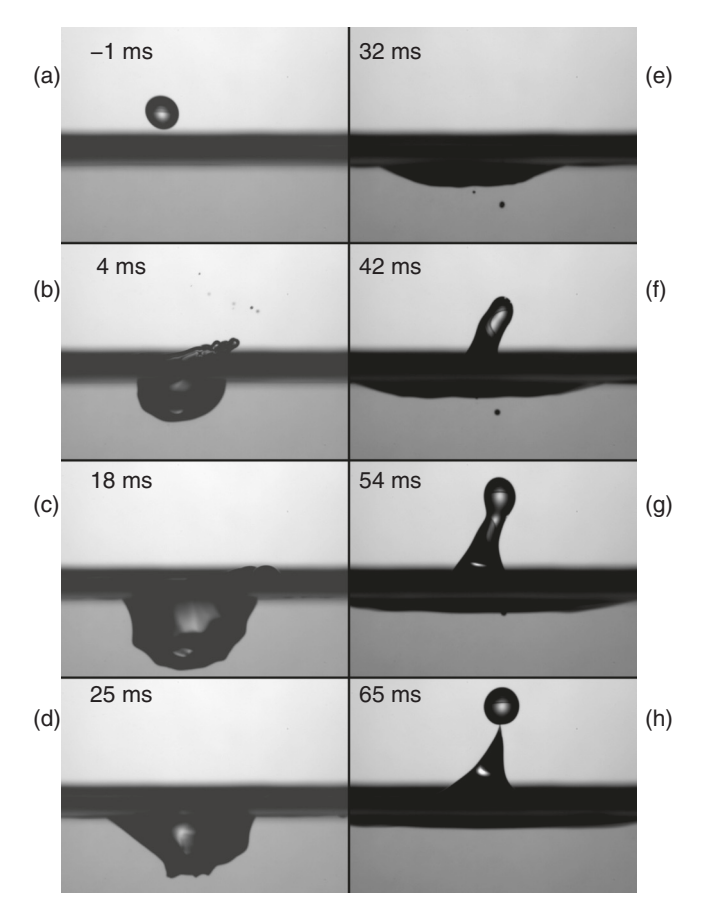


FIG. 5. Images from the high-speed movie of the oblique impact of a single drop on the deep-water surface with a wind speed of 4.5 m/s. Each image shows a  $28.6 \times 21.4$  mm<sup>2</sup> section and the wind is blowing from left to right. The time in milliseconds refers to the frame just before the drop impact (t = 0 ms). The diameter of the primary drop is D = 3.3 mm, the impact angle is  $\theta = 13.3^{\circ}$ , the vertical and horizontal impact velocities are v = 2.0 and u = 0.45 m/s, respectively, and We = 171.

### A. Qualitative results of wind effects on the cavity and central jet

Figure 5 shows eight images of a cavity [the crater, Figs. 5(b)-5(d)] and central jet [the stalk, Figs. 5(f)-5(h)] from the high-speed movie of a single drop impact with a wind speed of  $U_w = 4.5 \text{ m/s}$ . Figure 6(a) shows the shape-profile history of the crater extracted from the same movie before the crater reaches its greatest depth, while Fig. 6(b) shows the contour histories of the crater and the stalk from the moment of the greatest crater depth to the maximum height of the stalk. In these figures, the wind propagates from left to right and the drop impinges on the water surface with an angle of  $13.3^{\circ}$  from the vertical. The thick air-water interface with blurred edges in each individual image in Fig. 5 is due to the effects of the meniscus, formed at the interface between the liquid surface and the sidewalls of the test section. As can be seen in Fig. 5(b), shortly after initial impact, the cavity forms underneath the original quasiflat water surface at the impact location and is slightly asymmetrical along the wind direction. At this moment, an asymmetrical crown is indicated by a tilted protuberance that is visible above the water surface on the leeward side of the cavity rim. A number of small secondary droplets appear right above the crown. (The large dark secondary droplet is near the focal plane of the camera, while the small fuzzy ones are certain distances away from the focal plane.) As the impact process continues, the cavity walls move downward and outward and the

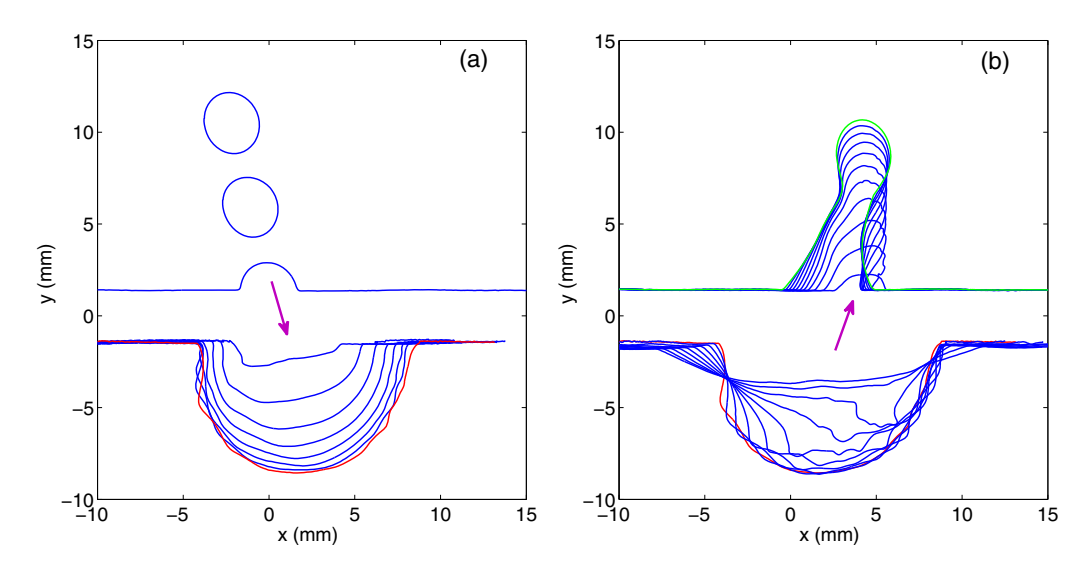


FIG. 6. Contour profile histories of the cavity and stalk from the same movie as the images shown in Fig. 5. (a) Growth phase of the cavity from the moment 4 ms prior to the drop impact to the maximum depth, t = 18 ms (red line), and (b) collapse phase of the cavity from the moment of maximum depth (red line) and the growth phase of the stalk until the maximum height (green line). Here x = 0 is the impact center and y = 0 corresponds to the free water surface. The time between profiles is 2 ms. The horizontal line portions of the cavity and stalk contours are the bottom and top of the meniscus on the tank wall, respectively.

cavity becomes more asymmetrical as the steepness of the cavity wall on the windward side is greater than that on the leeward side [see Fig. 6(a)]. The penetration velocity of the cavity at the beginning of impact is about 1.28 m/s, measured from the distance between the first two cavity contours along the impact direction divided by the time involved. During the outward motion of the cavity walls, the left edge of the cavity on the windward side of the impact site travels about 2 mm, which is much less than that on the leeward side (about 5 mm). Capillary waves that originated from the cavity rim [both corners of the crater wall near the free water surface; see Fig. 6(a)] start to propagate downward along the cavity wall. Both the amplitude and propagation speed of the capillary waves on the windward side are greater than that on the leeward side. As the capillary waves reach the cavity bottom, the cavity shape is distorted and a cusp forms near the left corner of the cavity bottom [Fig. 5(d), t = 25 ms]. A bubble is generated at the tip of the cusp (not shown in the image). As the crater retreats upward, the cusp and capillary waves continue to propagate in the wind direction and the cusp becomes more pronounced until it reaches the opposite side of the cavity wall [see Fig. 6(b)]. During the retreat of the crater, the cavity rim on the windward side of the impact site travels a much larger distance than that on the leeward side.

At t = 32 ms after initial impact, the crater disappears and a couple of air bubbles are left underneath the water surface [Fig. 5(e)]. A little while later, a central jet (stalk) forms on the original impact site. The initial width of this jet is approximately 4 mm. The jet moves upward and slows down as it rises [Fig. 6(b)]. It is interesting to note that while the stalk shown in the image [Figs. 5(f) and 5(g)] tilts to the leeward side, the highest point of each stalk contour in the stalk shape-profile history moves strictly upward [Fig. 6(b)]. Also, Fig. 6(b) shows that while the leeward side of the stalk base is stationary, the windward side of the stalk base propagates in the windward direction and as a result the center of the stalk base shifts to the windward direction. As the stalk approaches its greatest height [Fig. 5(h)], a droplet comparable in size to the impacting drop forms on the top of the stalk and a little while later this droplet separates from the stalk tip and becomes a secondary drop. The secondary drop continues to move upward until its greatest height is reached. Both the secondary drop and the rest of the stalk fall back to the water surface eventually due to gravity.

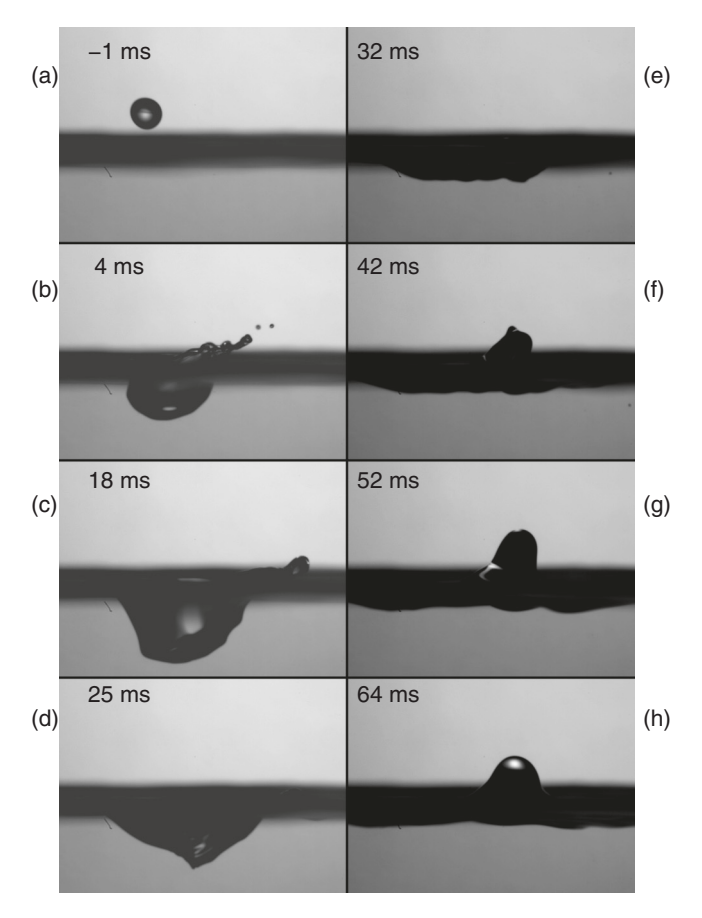


FIG. 7. Images from the high-speed movie of the oblique impact of a single drop on the deep-water surface with a wind speed of 6.0 m/s. Each image shows a  $28.6 \times 21.4$  mm<sup>2</sup> section and the wind is blowing from left to right. The time in milliseconds refers to the frame just before the drop impact (t = 0 ms). The diameter of the primary drop is D = 3.1 mm, the impact angle is  $\theta = 25.3^{\circ}$ , the vertical and horizontal impact velocities are v = 1.9 m/s and u = 0.9 m/s, respectively, and We = 183.

Figure 7 shows eight images of the crater [Figs. 7(b)–7(d)] and the stalk [Figs. 7(f)–7(h)] from the high-speed movie of a single drop impact with a wind speed of  $U_w = 6.0$  m/s. In the figure, the diameter of the primary water drop is D = 3.1 mm and the angle of impact is  $\theta = 25.3^{\circ}$ . Figure 8 shows the contour histories of the crater and stalk from the same movie as shown in Fig. 7. Comparing Figs. 7 and 8 with Figs. 5 and 6, one can see that the aforementioned phenomena of the drop impact are changed both quantitatively and qualitatively. First, the crown on the leeward side of the cavity rim is much bigger in size than that in the previous case. Second, the asymmetrical shape of the cavity along the wind direction becomes even more pronounced. Third, the location of the cusp is closer to the cavity bottom. Fourth, a wider stalk, about 5 mm in diameter, forms and the maximum stalk height is reduced significantly. Finally, no secondary droplet is generated from the tip of the stalk.

It should be mentioned that the meniscus (the thick air-water interfaces with blurred edges in the images of Figs. 5 and 7) obscures the part of the image that is close to the air-water interface, resulting in incomplete measurements of crowns and secondary droplets. Thus, the quantitative analysis of both crowns and secondary droplets is extremely difficult and beyond the scope of the present study.

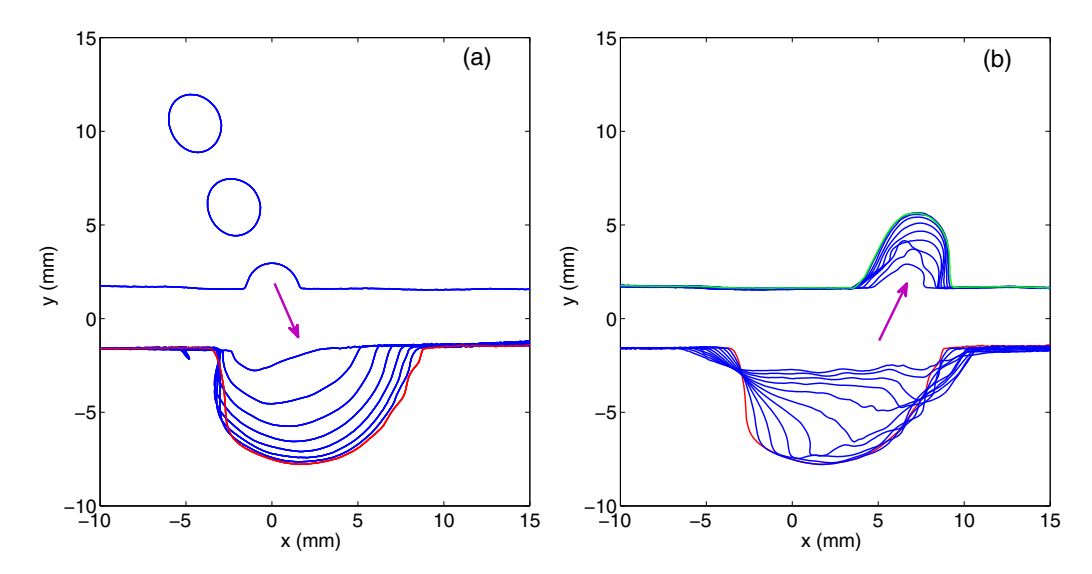


FIG. 8. Contour profile histories of the cavity and stalk from the same high-speed movie as the images shown in Fig. 7, for the oblique impact of a single drop on the deep-water surface with a wind speed of 6.0 m/s. (a) Downward movement of the cavity, from the moment 4 ms prior to the drop impact to the maximum depth, t = 18 ms (red line), and (b) retreat of the cavity from the moment of maximum depth (red line) and upward movement of the stalk until the maximum height (green line). Here x = 0 is the impact center and y = 0 corresponds to the free water surface. The time between profiles is 2 ms. The horizontal line portions of the cavity and stalk contours are the bottom and top of the meniscus on the tank wall, respectively.

In the following sections, only cavities, capillary waves, and stalks (central jets) with different wind speeds are discussed.

# B. Cavity and capillary waves

Figure 9 shows the temporal evolution of the vertical and horizontal positions of the deepest point on the contour profile of the cavity under various wind conditions. In Fig. 9(a), the horizontal axis is the cavity elapsed time, scaled by the vertical impact velocity with the drop diameter, while the vertical axis, with the positive direction upward, depicts the cavity depth scaled by the drop diameter. As can be seen from Fig. 9(a), at the beginning of the cavity expansion (tv/D < 5), all three curves collapse into a single curve that follows the asymptotic solution of the temporal evolution of the crater depth for normal drop impact [21]. This indicates that the wind has little effect on the penetration depth of the cavity during the early expansion of the cavity. After the maximum cavity depth is reached, the cavities in the wind field retract faster than in the case of no wind. Figure 9(b), in contrast, shows that the temporal revolution of the horizontal displacement of the cavity may be divided into three phases, corresponding to the cavity expansion, maximum depth, and retraction. As can be seen from Fig. 9(b), the initial position of the deepest point of the cavity contour in each case is located on the windward side of the cavity ( $d_{\text{cavt}} < 0$ ). During the early expansion of the cavity, i.e., phase 1, the bottom of each cavity moves toward the leeward direction with nearly a constant speed (lines with a nearly constant slope). At the instant labeled by A in Fig. 9(b), the displacement of the cavity's bottom reaches a value of about 0.5D. After instant A, the lowest point of the cavity contour moves back and forth around 0.5D along the wind direction until the instant labeled by B. This oscillation in phase 2 is due to the passage of capillary waves through the bottom of the cavity. In phase 3 (after instant B), the lowest point of the cavity contour moves toward the leeward side at a faster rate than in phase 1. The movement of the cavity in phase 3 is dominated by the bulge-capillary-waves pattern that is discussed in the latter part of this section.

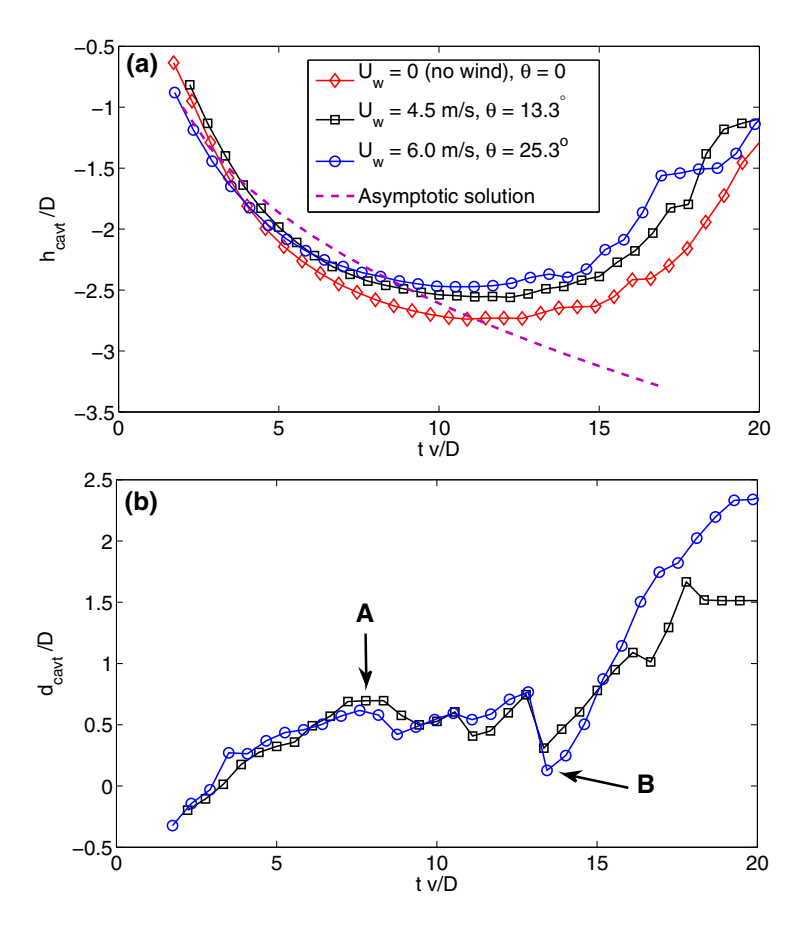


FIG. 9. (a) Cavity depth  $h_{\rm cavt}$  and (b) displacement  $d_{\rm cavt}$  as a function of time under various wind conditions. Here t=0 corresponds to the moment of the drop impact, v is the vertical impact velocity of the primary drop, and the diameters D of the primary drops corresponding to  $U_w=0,4.5$ , and 6.0 m/s are 3.5, 3.3, and 3.1 mm, respectively.

In light of the cavity below the free water surface, it is conjectured that the aforementioned behaviors of the cavity are dominated by oblique impact. Based on the experimental data of the oblique impact of drops on a deep liquid pool, Ref. [30] predicted that the maximum penetration depth of the cavity  $h_m$  depends on the vertical impact velocity v and can be approximately given by

$$\frac{h_m}{D} = 0.18 \,\text{We}_v^{1/2},\tag{1}$$

where  $We_v = \frac{\rho v^2 D}{\sigma}$  is the vertical Weber number. Figure 10 shows a plot of  $\frac{h_m}{D}/We_v^{1/2}$  as a function of the impact angle  $\theta$ . As can be seen from the figure, over the whole range of  $\theta$  studied,  $\frac{h_m}{D}/We_v^{1/2}$  is nearly a constant of around 0.2, which is very close to the 0.18 that is given in Eq. (1). It should be mentioned that while the wide range of  $We_v$  is used in [30] by varying the impact velocity and impact angle, i.e.,  $v = U \cos \theta$  with a nearly constant drop diameter (around 100  $\mu$ m), a very limited range of  $We_v$  is used herein because the vertical impact velocity v is almost the same due to the constant release height of the primary drop. Also, the shape of the cavity reported in Ref. [30] is quite different from that in the present experiment. In [30], the cavity at its maximum dimensions has a sharp bottom tip extending in the direction of drop impact, while the bottom of the cavity herein is round [see Fig. 6(a)].

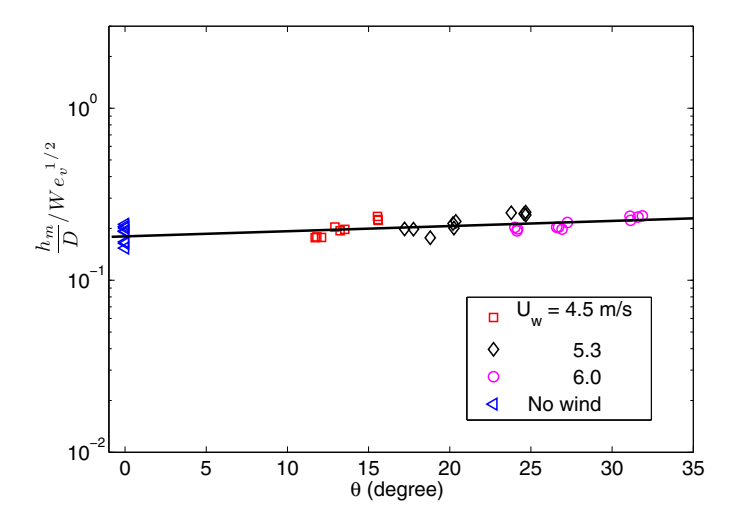


FIG. 10. Maximum crater depth  $h_m$  as a function of the impact angle of the primary drop under various wind conditions.

Figure 11 shows the behaviors of capillary waves on the surface of the cavity during the retraction of the cavity. The cavity-contour profile data are from Fig. 6(b). In the figure, each successive contour profile of the cavity is plotted 1/2 mm above the previous profile to avoid overlapping curves. The time between two consecutive profiles is 1 ms. The bottom red curve is the cavity contour extracted from the image at the instant the cavity reaches the maximum depth. This instant is defined as the first image of the time sequence (j = 1). To obtain the actual height of the jth contour profile from the plot, one reads the height from the vertical axis and then subtracts (j-1)/2 mm. The last (top) profile shows the central jet forming on the water surface and the large gap between the last two profiles is due to the meniscus on the tank wall. The dashed curve is a semiellipse computed with the maximum depth and radius of the cavity for normal impact, as described in [23]. As can be seen from Fig. 11, at the instant the cavity reaches its maximum depth, the shape of the cavity contour (the red curve) is very similar to that for normal impact (the dashed curve), except that there is a large bulge with a rather sharp outer corner, called the toe, on the windward side near the free water surface. As the cavity continues to retract upward, the toe propagates in the wind direction and downward along the surface of the cavity [see Fig. 6(b)] and eventually becomes the lowest point of the cavity surface [at instant B shown in Fig. 9(b)]. The horizontal velocity of the toe might be determined by the slope using the data points after instant B in Fig. 9(b) and this velocity increases as the impingement angle  $\theta$  increases. Figure 11 also shows that two capillary waves appear upstream of the toe. These capillary waves become shorter in wavelength during the retraction of the cavity. It is speculated that the tangential local velocity of the underlying flow in the reference frame of the toe is slower than the minimum phase speed of linear capillary-gravity waves, according to the theory of capillary jump proposed in [49]. However, the calculation of tangential local flow velocity with the theory is not a simple matter since the theory is for a two-dimensional steady wave while the capillary waves in the present study are on the three-dimensional curved crater wall.

In addition, Fig. 11 shows that the retracting velocity of the surface on the leeward side of the cavity is much slower than that on the windward side. This might be explained by the fact that the retracting direction of the cavity surface on the leeward side is opposite to the direction of the drop impact. Capillary waves without a companion bulge on the leeward side surface are nearly stationary relative to the free water surface during the retraction of the cavity.

It is interesting to notice that all capillary waves gradually merge into the windward-side toe to focus the kinetic energy of the fluid. The focusing point shifts to the leeward side. Later, a central jet forms above the focusing point on the water surface and its distance relative to the impact position

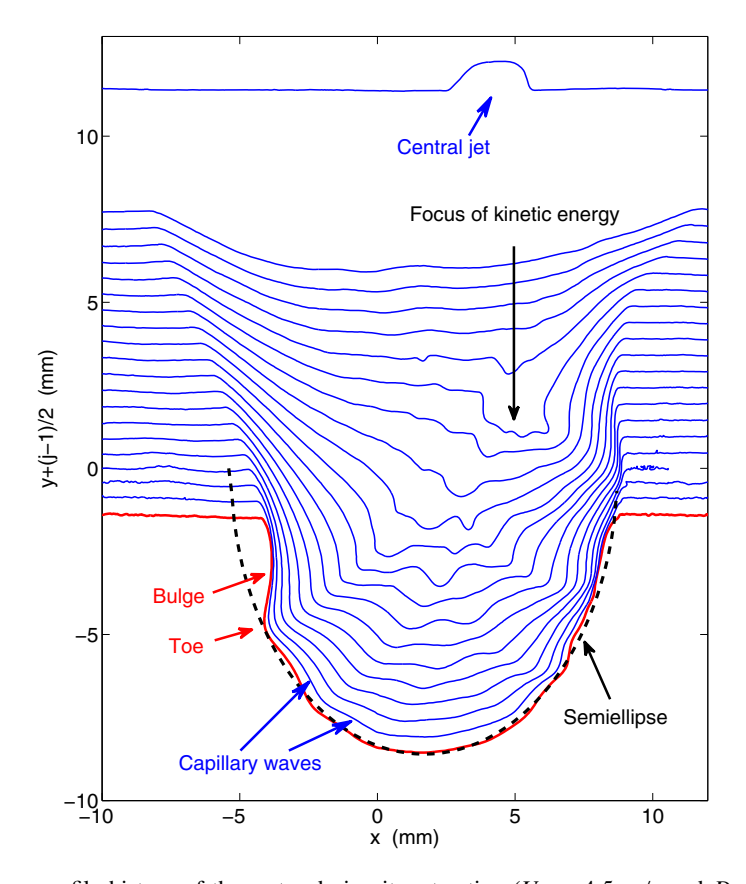


FIG. 11. Shape profile history of the crater during its retraction ( $U_w = 4.5 \text{ m/s}$  and D = 3.3 mm). The profile data are from Fig. 6(b). The bottom red curve is the crater contour at the moment the crater reaches the maximum depth, defined as the first image of the time sequence (j = 1), while the dashed curve is a semiellipse for normal impact, as described in [23]. Each successive profile is plotted 1/2 mm above the previous profile for clarity and the time between profiles is 1 ms. The top profile shows the central jet formed on the water surface and the big gap between the last two profiles is due to the meniscus on the tank wall.

(x = 0) increases as the wind velocity increases [comparing Fig. 6(b) with Fig. 8(b)], indicating that the bulge and capillary waves play important roles in the formation of the central jet. The mechanisms of the aforementioned asymmetrical characteristics of the bulge and capillary waves on the cavity surface are not immediately clear. Further investigations are expected.

## C. Maximum height of the central jet (the stalk height)

Figure 12 shows three contours of central jets with various wind velocities at the moment these central jets reach their maximum heights, the so-called stalk height. As can be seen from the figure, as the wind speed increases, the stalk height decreases drastically and the location of the stalk (central jet) shifts to the leeward side (the wind blows from left to right) by about 7 mm for the case with a wind speed of 6.0 m/s. The shifting of the position of the central jet leeward is mainly due to the effects of wind on the bulge and capillary waves that propagate along the cavity wall, as described in the preceding section. Additionally, as was shown in Figs. 4 and 7, for the case of no wind the central jet breaks up at the moment it reaches the maximum height and a secondary drop forms on the jet tip. There is no breakup of the central jet for the case of a high wind speed of 6.0 m/s.

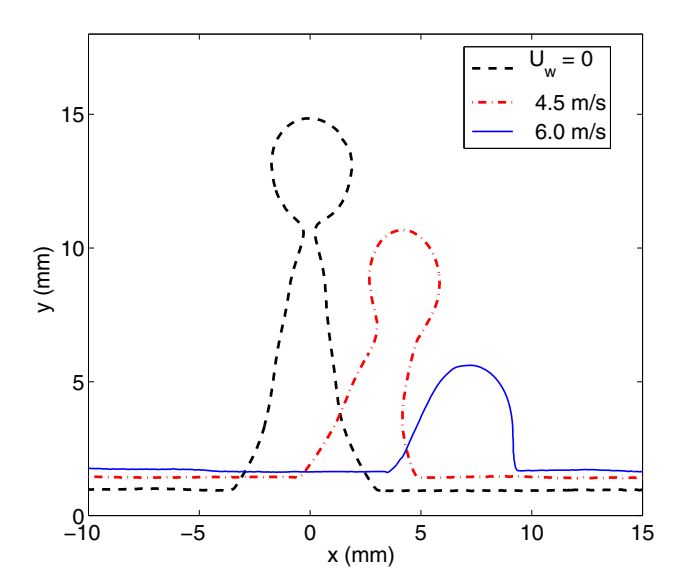


FIG. 12. Contours of the stalk at the moment they reach the maximum heights. The case of  $U_w = 0$  corresponds to the normal impact (without wind) and the origin is the impact center at the free water surface. The horizontal line portions of the stalk contours are the top of the meniscus. The diameters of the primary drops corresponding to  $U_w = 0$ , 4.5, and 6.0 m/s are 3.5, 3.3, and 3.1 mm, respectively.

Two sets of parameters are involved in describing the behavior of the stalk height. One set includes quantities of the primary drop, i.e., the diameter D, density  $\rho$ , gravity g, horizontal velocity u, vertical velocity v, surface tension  $\sigma$ , and viscosity  $\mu$ , while the other set includes quantities of the wind field, i.e., the air density  $\rho_a$ , air viscosity  $\mu_a$ , and wind speed  $U_w$ . Herein, we also use the velocity magnitude ( $U = \sqrt{u^2 + v^2}$ ) and impingement angle [ $\theta = \tan^{-1}(\frac{u}{v})$ ] of the primary drop. The range of U varies from 1.89 to 2.25 m/s, while  $\theta$  ranges from 0 to 40° from the vertical. Note that the angle of the drop impact  $\theta$  in the wind field can be determined by the Froude number based on the wind speed  $\mathrm{Fr}_w = U_w^2/gD$ , as shown in the Appendix. The surface tension of the primary drop and the water in the pool is  $\sigma = 73$  mN/m, as the experiment was performed at room temperature. Thus, the Froude number based on the impact velocity of the primary drop  $\mathrm{Fr} = U^2/gD$  covered in the present paper is in a limited range of 100–202 while the Weber number  $\mathrm{We} = \rho U^2 D/\sigma$  ranges from 142 to 256.

The effects of impact velocity, surface tension, and viscosity on the breakup of central jet for normal impact have been experimentally investigated in [24]. It is shown that the central jet breaks up in a regime where  $Oh \leq 0.091$  combined with the Weber numbers beyond certain critical values. As for the present data, Oh varies from 0.0022 to 0.0026 and the values of We are beyond the critical value in water. In the case of no wind (normal impact) and a number of cases of low wind speeds with large drop diameters, central jets break up. It is found that the breakup boundary of these jets is determined by the wind Froude number  $Fr_w$ , in addition to We and Oh. The breakup of the central jet occurs when the  $Fr_w$  is less than approximately 700.

As for normal drop impact, corresponding to the case of no wind ( $U_w = u = \theta = 0$ ) in the present study, Ref. [13] showed that the stalk height produced by the impact of large drops on a liquid surface is a function of Fr as follows:

$$\frac{H}{D} = 1.43 \,\text{Fr}^{1/4}.\tag{2}$$

As shown by Eq. (2), the current range of Fr (100 < Fr < 202) to the one-fourth power produces a very limited variation of H/D, indicating that the effect of the Froude number Fr on the present stalk

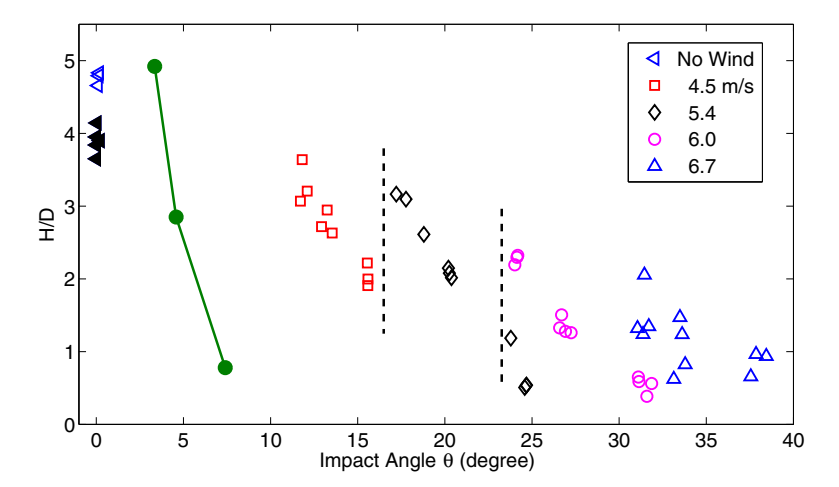


FIG. 13. Nondimensional maximum stalk height H/D versus the impact angle  $\theta$  of the primary drop. The data points for the case of no wind ( $\theta = 0$ ) are divided into two groups, corresponding to different types of jets [23]:  $\triangleleft$ , a slow thick (Worthington) jet;  $\blacktriangleleft$ , a fast thin jet. Three closed circles connected by a green line are the experimental data of normal impacts on horizontally moving films estimated from [39]. The data points around the two vertical bars show that H/D increases with increasing wind speed.

height data is minor. A similar conclusion can be drawn for the Weber number We, since We =  $2l_c^2$ Fr, where  $l_c = \sqrt{2\sigma/\rho g}/D$  is the dimensionless capillary length with a narrow range of 0.94 to 1.54 in the present paper. In addition, the effect of the water viscosity on the stalk height can be neglected, as discussed in [13,23].

Figure 13 shows the nondimensional stalk height H/D varying with the impingement angle  $\theta$  of the drop impact. In the figure, the data points for the case of no wind (normal impact,  $\theta = 0$ ) are divided into two groups because of the two different mechanisms of jet formation, as discussed in [23]. The data points ( $\triangleleft$ ) around 4.6 correspond to the slow thick (Worthington) jets that are caused by cavity retraction and follow Eq. (2). In contrast, the data points (◄) with low values around 4 correspond to the fast thin jet that is produced by the collapse of a singular capillary wave and a number of secondary drops are ejected from the jet tip prior to the maximum jet height. It should be mentioned that this fast thin jet was not observed in all wind cases  $(U_w > 0)$  reported herein. (This was verified by a second high-speed camera that viewed the impact process from the top [43].) It is conjectured that the absence of the fast thin jet in the wind field may be because the collapse of the focusing capillary wave is impeded by a nonaxisymmetric distortion in the shape of capillary waves. Thus, in the following discussion, we focus mainly on the slow thick (Worthington) jet caused by cavity retraction in the wind field. In addition, the experimental data of normal impacts on horizontally moving water films (data points connected by the green line) are also included in Fig. 13, for the sake of comparison. These data points are calculated from Fig. 8 of [39], where the jet height is essential as a function of the height of the moving film and the Weber number (the impact velocity). The data points with the film height of 9.3 mm (the deepest water film) are chosen and a drop diameter of 3.86 mm was used in our calculation. It should be noted that no information is available in the literature on the central jet (stalk) caused by the oblique impact of a drop onto a static liquid surface.

As can be seen from Fig. 13, H/D decreases with increasing  $\theta$ , indicating that the oblique drop impact caused by the wind plays a major role in the dynamics of the stalk height. However, for a given impact angle of the primary droplet, the nondimensional stalk height increases as the wind speed increases (comparing the data points around the two vertical bars). This variation in the data indicates that H/D must be strongly influenced by the wind drag force in addition to the impingement angle of drop impact.

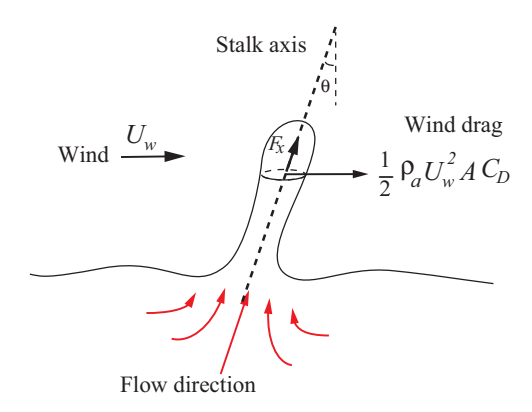


FIG. 14. Schematic showing the growing stalk in the wind field.

A schematic showing the wind drag force acting on the top part of a growing stalk above the water surface is given in Fig. 14. As can be seen from the figure, the component of the drag force in the axial direction of the stalk contributes to the growth of the stalk height and may be approximated by

$$F_x \sim \frac{1}{2} \rho_a U_w^2 A C_D \sin \theta, \tag{3}$$

where  $\rho_a$  is the air density,  $U_w$  is the wind velocity,  $C_D$  is the drag coefficient, A is the characteristic area of the stalk, and  $\theta$  is the inclined angle of the stalk axis relative to the vertical. It is well known that the drag coefficient  $C_D$  for a flow over a sphere and cylinder is a function of Reynolds number  $(\text{Re} = \rho_a U_w D/\mu_a)$ , where  $\rho_a$ ,  $\mu_a$ , and  $U_w$  are the air density, air viscosity, and wind speed, respectively. For a laminar boundary layer with small Re (less than 1000),  $C_D \propto \text{Re}^{-1}[50]$ . Measurements of the peak locations of first three or four consecutive contour profiles of the central jet reveal that the inclined angle of the stalk can be approximated by the incidence angle of the drop impact, for example, comparing the two vectors in Figs. 6(b) and 8(b) with those in Figs. 6(a) and 8(a), respectively. For small  $\theta$ ,  $\sin \theta \sim \theta$ . Thus, from Eq. (3),  $F_x \propto \theta \, \text{Re}^{-1}$ , indicating that the nondimensional stalk height H/D depends on  $\theta \, \text{Re}^{-1}$  as well.

Figure 15 shows the nondimensional stalk height H/D varying with  $\theta \, \mathrm{Re}^{-1}$  by using the experimental data shown in Fig. 13. As can be seen from the figure, the data collapse to a single curve and H/D decreases with increasing  $\theta \, \mathrm{Re}^{-1}$  in a nonlinear fashion until zero at  $\theta \, \mathrm{Re}^{-1} = 0.03$  and then increases for  $\theta \, \mathrm{Re}^{-1} > 0.03$ . The increase of H/D for large  $\theta \, \mathrm{Re}^{-1}$  is likely to be an indication that the effects of Re are dominant for high wind speeds. Using a curve fit to the data for  $0 < \theta \, \mathrm{Re}^{-1} < 0.03$  yields

$$H/D = 4.52 - 303 \left(\frac{\theta}{\text{Re}}\right)^{1.2},$$
 (4)

with the coefficient of determination  $R^2=0.94$ . As shown by the different exponent signs in the equation, the dimensionless stalk height decreases with increasing impingement angle  $\theta$ , but increases as the Reynolds number Re increases. It is worth recalling that the relationship given in Eq. (4) is obtained under the condition of a small range of the Froude number ( $100 \le \text{Fr} \le 202$ ). Also, note that Eq. (4) is valid for Re = 0 ( $U_w=0$ ) because  $\theta \text{ Re}^{-1}=0$  with  $\theta \sim \text{Fr}_w$  (see the Appendix). The coefficient 4.52 in Eq. (4) is approximately equal to that computed from Eq. (2) with Fr = 100 for normal drop impact.

The phenomenon of inclined stalks has been observed in a normal drop impact on horizontal moving films given in [39]. In this paper, Figs. 6 and 7 show the stalks (central jets) generated by the impact of a droplet with a diameter of 3.86 mm on a 7.9-mm-deep moving water film with an average velocity of  $u_f = 0.17$  m/s. The impact velocities of the droplet in these two figures are 1.9 and 2.94 m/s, respectively. The stalks are inclined in the same direction as that of the film flow. As

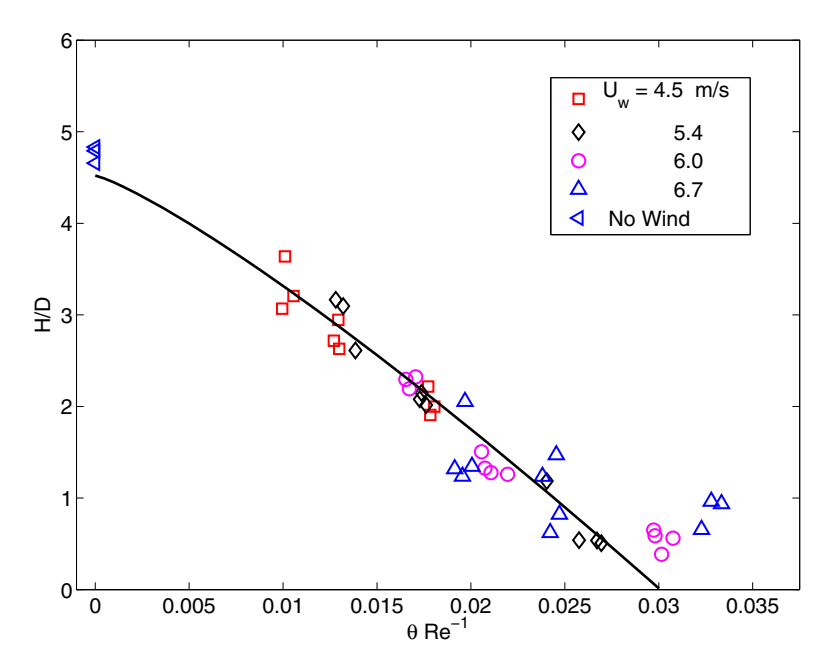


FIG. 15. Nondimensional stalk height H/D varying with  $\theta$  Re<sup>-1</sup> with the experimental data shown in Fig. 13. For clarity, only slow thick (Worthington) jets for the case of no wind are included in this figure. The solid curve is Eq. (4) and  $\theta$  is in degrees.

the stalks continue to rise, the inclined angles of the stalks relative to the vertical decrease and the stalks eventually become very close to the vertical, due to the movement of the stalk base with the target film. Figure 6 of [39] also shows that the inclined angle of the stalk with respect to the vertical reaches approximately  $21^{\circ}$  at t=34 ms after the drop impact, while the incidence angle of the drop impact is only  $5.12^{\circ}$ . In contrast, the inclined direction of the stalks reported in the present paper is the same as that of the wind, i.e., the horizontal direction of primary drop motion in the air. This is opposite to the relative direction of the oblique drop impact with respect to the flow film given in [39].

#### IV. CONCLUSION

In the present experiments, the effects of wind on the impacts of single water drops on a deep-water surface were studied. Different experiments were performed with varying impacting drop sizes, ranging from 2.5 mm to 4.1 mm and wind speeds up to 6.7 m/s. The horizontal velocities of drop impacts varied from 0 to 1.4 m/s while the vertical velocities were kept nearly the same (about 2.0 m/s). Within the range of the studied parameters, both the cavity and central jet always occurred during the drop impacts. These events were recorded with a backlit cinematic shadowgraph technique that uses a high-speed camera in the lateral perspective.

The experimental results show that shortly after the primary drop hits the water surface, an asymmetrical cavity appears along the wind direction, with a train of capillary waves on the cavity wall. This is followed by the formation of an inclined central jet at the location of the drop impact. It was found that the wind has little effect on the penetration depth of the cavity at the early stage of the cavity expansion, but markedly changes the capillary waves during the retract of the cavity. The capillary waves shift the position of the central jet formation to the leeward side. The displacement of the central jet formation increases as the wind velocity increases.

The dynamics of the central jet are dominated by two mechanisms: (i) the oblique drop impact produced by the wind and (ii) the wind drag force directly acting on the jet. The breakup of the

central jet may be determined by the wind Froude number  ${\rm Fr}_w=U_w^2/gD$ , in addition to the Weber and Ohnesorge numbers. The stalk height is drastically affected by the wind, as the nondimensional stalk height H/D decreases with increasing  $\theta$  Re<sup>-1</sup> in a nonlinear fashion. Here  $\theta$  is the impingement angle of the drop impact in the wind field and may be determined by  ${\rm Fr}_w$ , while  ${\rm Re}=\rho_a U_w D/\mu_a$  is the Reynolds number with air density  $\rho_a$ , wind speed  $U_w$ , and air viscosity  $\mu_a$ .

It should be mentioned that with the current experimental facility, impacting drops with zero initial velocity are generated in the wind field. Thus, the impingement angle of the drop impact is strongly correlated with the wind velocity and drop diameter, as shown in the Appendix. This correlation is unnecessary in certain natural phenomena and industrial applications. For future work, experiments with the impingement angle of drop impact independent of wind velocity are suggested. This may be accomplished by varying the initial vertical velocity of primary drops. The effects of surface tension and viscosity on the dynamics of central jets caused by oblique impact in the presence of wind should be considered. Also, the development of certain techniques to produce a single large droplet with variable initial velocity in both horizontal and vertical directions is expected.

#### ACKNOWLEDGMENTS

The authors would like to thank Dr. James H. Duncan for his numerous suggestions and Dan Wang, Ren Liu, and Junyi Li for their assistance with taking measurements and processing the data. Constructive comments from two anonymous reviewers strengthened the paper. This work was supported by the Division of Ocean Science, National Science Foundation, under Award No. 0962107.

#### APPENDIX: INCIDENCE ANGLE OF DROP IMPACT IN THE WIND FIELD

As the primary droplet of diameter D falls in the wind field, the drag force in the horizontal direction due to wind may be given by

$$F_D = \frac{1}{2}\rho_a (U_w - u)^2 C_D A,$$
 (A1)

where  $\rho_a$  is the air density,  $U_w$  is the wind velocity, u is the horizontal velocity of the primary droplet,  $C_D$  is the drag coefficient, and  $A = \frac{\pi}{4}D^2$  is the cross-sectional area of the primary droplet. Thus, the horizontal acceleration of the primary droplet with a mass of  $m = \rho_w \frac{\pi}{6}D^3$  in the wind field is

$$a_h = \frac{F_D}{m} = \frac{3}{4} C_D \frac{\rho_a}{\rho_w} \frac{(U_w - u)^2}{D}.$$
 (A2)

Similarly, the vertical acceleration of the primary droplet due to gravitational, air drag and buoyancy forces may be given by

$$a_v = g - \frac{3}{4} C_D \frac{\rho_a}{\rho_w} \frac{v^2}{D} - \frac{\rho_a}{\rho_w} g,$$
 (A3)

where  $g = 9.81 \text{ m/s}^2$  is the gravitational constant and v is the vertical velocity of the primary droplet. Since  $\rho_a \ll \rho_w$  and u and v are relatively small due to the short traveling distance ( $\sim 0.254 \text{ m}$  in the vertical) of the primary drops, Eqs. (A2) and (A3) may be approximated by

$$a_h \approx \frac{3}{4} C_D \frac{\rho_a}{\rho_w} \frac{U_w^2}{D}, \quad a_v \approx g.$$
 (A4)

With zero initial velocity of the primary droplet, the incidence angle of the drop impact on water surface in the wind field may be represented as follows:

$$\theta = \tan^{-1}\left(\frac{a_h}{a_v}\right) = \tan^{-1}\left(\frac{3}{4}C_D\frac{\rho_a}{\rho_w}\frac{U_w^2}{gD}\right). \tag{A5}$$

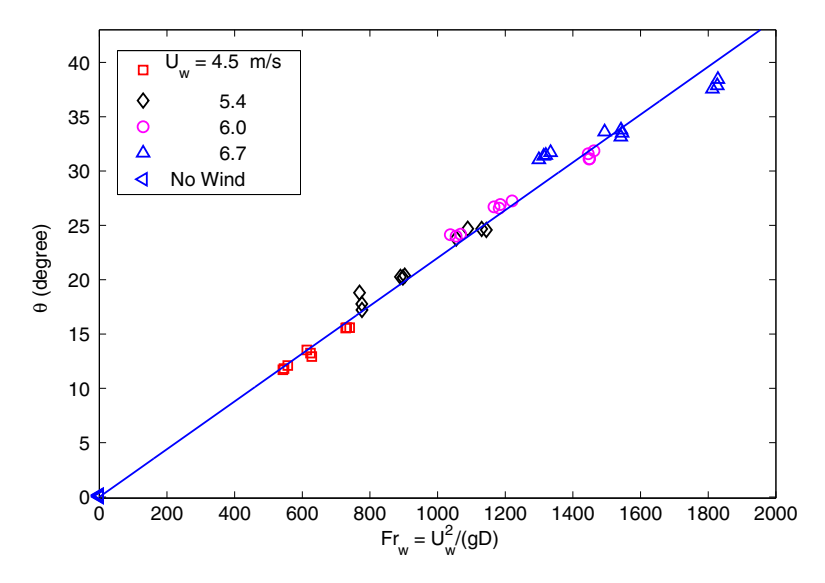


FIG. 16. Drop impact angle  $\theta$  varying with the Froude number  $\text{Fr}_w = U_w^2/gD$ . The solid curve is Eq. (A6):  $\theta = 0.022 \, \text{Fr}_w$ .

By using 
$$\rho_a = 1.23 \text{ kg/m}^3$$
,  $\rho_w = 1000 \text{ kg/m}^3$ , and  $C_D = 0.43 \text{ for Re} = O(10^3)$ , Eq. (A5) becomes 
$$\theta = \tan^{-1}(3.97 \times 10^{-4} \text{Fr}_w) \approx 0.022 \text{ Fr}_w, \tag{A6}$$

where  $\theta$  is in degrees and  $\operatorname{Fr}_w = \frac{U_w^2}{gD}$  is the wind Froude number, defined as the ratio of aerodynamic forces to the gravitational force. As can be seen from Eq. (A6), the incidence angle of the drop impact increases as the wind velocity increases. For a given wind velocity, the incidence angle of the drop impact decreases as the diameter of the primary drop increases. Figure 16 shows that Eq. (A6) is in good agreement with the results computed with  $\theta = \tan^{-1}(\frac{u}{v})$  based upon the present measurements in our laboratory.

It should be mentioned that Eq. (A6) would change if there existed a nonzero initial velocity for the primary drop after leaving the needle tip. Also, it is difficult to produce a primary droplet of nonzero initial velocity with the current techniques in our laboratory.

<sup>[1]</sup> J. A. Nystuen and D. M. Farmer, The influence of wind on the under-water sound generated by light rain, J. Acoust. Soc. Am. **82**, 270 (1987).

<sup>[2]</sup> M. Anguelova, R. P. Barber, and J. Wu, Spume drops produced by the wind tearing of wave crests, J. Phys. Oceanogr. 29, 1156 (1999).

<sup>[3]</sup> F. Veron, C. Hopkins, E. L. Harrison, and J. A. Mueller, Sea spray spume droplet production in high wind speeds, Geophys. Res. Lett. 39, L16602 (2012).

<sup>[4]</sup> A. M. Worthington, A Study of Splashes (Longmans, Green and Co., London, 1908).

<sup>[5]</sup> G. J. Franz, Splashes as sources of sound in liquids, J. Acoust. Soc. Am. 31, 1080 (1959).

<sup>[6]</sup> O. G. Engel, Crater depth in fluid impacts, J. Appl. Phys. 37, 1798 (1966).

<sup>[7]</sup> H. N. Oguz and A. Prosperetti, Bubble entrainment by the impact of drops on liquid surfaces, J. Fluid Mech. **219**, 143 (1990).

<sup>[8]</sup> A. Prosperetti and H. N. Oguz, The impact of drops on liquid surfaces and the underwater noise of rain, Annu. Rev. Fluid Mech. 25, 577 (1993).

- [9] M. Rein, The transitional regime between coalescing and splashing drops, J. Fluid Mech. 306, 145 (1996).
- [10] D. Morton, M. Rudman, and J. L. Liow, An investigation of the flow regimes resulting from splashing drops, Phys. Fluids 12, 747 (2000).
- [11] J. L. Liow, Splash formation by spherical drops, J. Fluid Mech. 427, 73 (2001).
- [12] S. L. Manzello and J. C. Yang, An experimental study of a water droplet impinging on a liquid surface, Exp. Fluids 32, 580 (2002).
- [13] A. I. Fedorchenko and A. B. Wang, On some common features of drop impact on liquid surfaces, Phys. Fluids 16, 1349 (2004).
- [14] Q. Deng, A. V. Anilkumar, and T. G. Wang, The role of viscosity and surface tension in bubble entrapment during drop impact onto a deep liquid pool, J. Fluid Mech. 578, 119 (2007).
- [15] B. Ray, G. Biswas, and A. Sharma, Generation of secondary droplets in coalescence of a drop at a liquid-liquid interface, J. Fluid Mech. 655, 72 (2010).
- [16] T. Tran, H. de Maleprade, C. Sun, and D. Lohse, Air entrainment during impact of droplets on liquid surfaces, J. Fluid Mech. 726, R3 (2013).
- [17] B. Ray, G. Biswas, and A. Sharma, Regimes during liquid drop impact on a liquid pool, J. Fluid Mech. **768**, 492 (2015).
- [18] M. Rein, Phenomena of liquid drop impact on solid and liquid surfaces, Fluid Dyn. Res. 12, 61 (1993).
- [19] H. C. Pumphrey and P. A. Elmore, The entrainment of bubbles by drop impacts, J. Fluid Mech. 220, 539 (1990).
- [20] L. V. Zhang, P. Brunet, J. Eggers, and R. D. Deegan, Wavelength selection in the crown splash, Phys. Fluids 22, 122105 (2010).
- [21] A. Bisighini, G. E. Cossali, C. Tropea, and I. V. Roisman, Crater evolution after the impact of a drop onto a semi-infinite liquid target, Phys. Rev. E 82, 036319 (2010).
- [22] E. Berberović, N. P. van Hinsberg, S. Jakirlić, I. V. Roisman, and C. Tropea, Drop impact onto a liquid layer of finite thickness: Dynamics of the cavity evolution, Phys. Rev. E **79**, 036306 (2009).
- [23] G. J. Michon, C. Josserand, and T. Séon, Jet dynamics post drop impact on a deep pool, Phys. Rev. Fluids 2, 023601 (2017).
- [24] E. Castillo-Orozco, A. Davanlou, P. K. Choudhury, and R. Kumar, Droplet impact on deep liquid pools: Rayleigh jet to formation of secondary droplets, Phys. Rev. E 92, 053022 (2015).
- [25] R. M. Schotland, Experimental results relating to the coalescence of water drops with water surfaces, Discuss. Faraday Soc. **30**, 72 (1960).
- [26] O. W. Jayaratne and B. J. Mason, The coalescence and bouncing of water drops at an air/water interface, Proc. R. Soc. London Ser. A **280**, 545 (1964).
- [27] S. L. Zhbankova and A. V. Kolpakov, Collision of water drops with a plane water surface, Fluid Dyn. 25, 470 (1990).
- [28] B. Ching, M. W. Golay, and T. J. Johnson, Droplet impacts upon liquid surfaces, Science 226, 535 (1984).
- [29] N. P. van Hinsberg and M. Charbonneau-Grandmaison, Single-drop impingement onto a wavy liquid film and description of the asymmetrical cavity dynamics, Phys. Rev. E 92, 013004 (2015).
- [30] M. V. Gielen, P. Sleutel, J. Benschop, M. Riepen, V. Voronina, C. W. Visser, D. Lohse, J. H. Snoeijer, M. Versluis, and H. Gelderblom, Oblique drop impact onto a deep liquid pool, Phys. Rev. Fluids 2, 083602 (2017).
- [31] G. Leneweit, R. Koehler, K. G. Roesner, and G. Schafer, Regimes of drop morphology in oblique impact on deep fluids, J. Fluid Mech. 543, 303 (2005).
- [32] T. Okawa, T. Shiraishi, and T. Mori, Effect of impingement angle on the outcome of single water drop impact onto a plane water surface, Exp. Fluids 44, 331 (2008).
- [33] B. Ray, G. Biswas, and A. Sharma, Oblique drop impact on deep and shallow liquid, Commun. Comput. Phys. 11, 1386 (2012).
- [34] P. Brambilla and A. Guardone, Automatic tracking of corona propagation in three-dimensional simulations of non-normal drop impact on a liquid film, Computing 95, 415 (2013).
- [35] P. Brambilla and A. Guardone, Assessment of dynamic adaptive grids in volume-of-fluid simulations of oblique drop impacts onto liquid films, J. Comput. Appl. Math. 281, 277 (2015).

- [36] M. Cheng and J. Lou, A numerical study of splash of oblique drop impact on wet walls, Comput. Fluids 115, 11 (2015).
- [37] H. Medwin, A. Kurgan, and J. A. Nystuen, Impact and bubble sound from raindrops at normal and oblique incidence, J. Acoust. Soc. Am. 88, 413 (1990).
- [38] X. Gao and R. Li, Impact of a single drop on a flowing liquid film, Phys. Rev. E 92, 053005 (2015).
- [39] S. K. Alghoul, C. N. Eastwick, and D. B. Hann, Normal droplet impact on horizontal moving films: An investigation of impact behavior and regimes, Exp. Fluids 50, 1305 (2011).
- [40] G. Liang, Y. Guo, Y. Yang, N. Zhen, and S. Shen, Spreading and splashing during a single drop impact on an inclined wetted surface, Acta Mech. 224, 2993 (2013).
- [41] Z. Che, A. Deygas, and O. K. Matar, Impact of droplets on inclined flowing liquid films, Phys. Rev. E 92, 023032 (2015).
- [42] J. R. Castrejón-Pita, B. N. Muñoz-Sánchez, I. M. Hutchings, and A. A. Castrejón-Pita, Drop impact onto moving liquids, J. Fluid Mech. 809, 716 (2016).
- [43] X. Liu, Experimental study of drop impact on deep water surface in the presence of wind, J. Phys. Oceanogr. 48, 329 (2018).
- [44] X. Liu, Q. Zheng, R. Liu, D. Wang, J. H. Duncan, and J. H. Huang, A study of radar backscattering from water surface in response to rainfall, J. Geophys. Res.: Oceans 121, 1546 (2016).
- [45] X. Liu, Q. Zheng, R. Liu, M. Sletten, and J. H. Duncan, A model of radar backscatter of rain-generated stalks on the ocean surface, IEEE Trans. Geosci. Remote Sens. 55, 767 (2017).
- [46] X. Liu and J. H. Duncan, An experimental study of surfactant effects on spilling breakers, J. Fluid Mech. **567**, 433 (2006).
- [47] A. B. Wang, C. C. Kuan, and P. H. Tsai, Do we understand the bubble formation by a single drop impacting upon liquid surface? Phys. Fluids 25, 101702 (2013).
- [48] M. Thoraval, Y. Li, and S. T. Thoroddsen, Vortex-ring-induced large bubble entrainment during drop impact, Phys. Rev. E 93, 033128 (2016).
- [49] M. S. Longuet-Higgins, Capillary jumps on deep water, J. Phys. Oceanogr. 26, 1957 (1996).
- [50] R. W. Fox and A. T. McDonald, Introduction to Fluid Mechanics, 3rd ed. (Wiley, New York, 1985).